Journal of Power Sources 630 (2025) 236084

Contents lists available at ScienceDirect

Journal of Power Sources

journal homepage: www.elsevier.com/locate/jpowsour

# A comprehensive study of phase evolution and electrochemical performance of the $Sr_{0.98}Ti_{0.5}Fe_{0.5}O_{3-\delta}$ perovskite as fuel electrode for steam electrolysis

Franziska E. Winterhalder [a], Yousef A. Farzin [c], Yoo Jung Sohn [a], Christian Lenser [a], Doris Sebold [a], Olivier Guillon [a,b,d], André Weber [c], Norbert H. Menzler [a,b,*]

[a] Institute of Energy Materials and Devices (IMD-2): Materials Synthesis and Processing, Forschungszentrum Jülich GmbH, 52425, Jülich, Germany
[b] RWTH Aachen University, Institute for Mineral Engineering (GHI), 52074, Aachen, Germany
[c] Institute for Applied Materials - Electrochemical Technologies (IAM-ET), Karlsruhe Institute of Technology (KIT), Adenauerring 20b, 76131, Karlsruhe, Germany
[d] JARA: Jülich-Aachen-Research-Alliance, 52425, Jülich, Germany

## HIGHLIGHTS

- STF perovskites with good chemical stability in SOEC conditions have been prepared.
- STF fuel electrode provided high electrocatalytic activity toward $H_2O$ electrolysis.
- Key degradation insights offer pathways to enhance long-term durability.

## ARTICLE INFO

*Keywords:*
STF fuel electrode
Perovskites
Electrochemical performance
Phase evolution
Steam electrolysis
Degradation mechanisms

## ABSTRACT

Perovskite-based electrodes have gained interest as alternatives to Ni-cermet fuel electrodes in solid oxide electrolysis cells (SOECs). This study investigates strontium-iron-titanate (STF) as a potential all-ceramic fuel electrode for SOECs. The chemical stability of pure STF during SOEC operating conditions at open circuit voltage (OCV) and the chemical reactivity between STF and yttria-stabilized zirconia (YSZ) under manufacturing and operation conditions are analyzed. The pure STF appears to be quite stable during SOEC operation. However, the STF and YSZ electrolyte powder mixture shows chemical interaction during manufacturing and operation conditions, confirming the need for a barrier layer between those two materials. Furthermore, the electrochemical performance of electrolyte-supported symmetrical and full cells is tested at different temperatures (650–800 °C) and steam concentrations (3–90 % $H_2O$). A mid-term degradation test in steam electrolysis operation for ca. 1700 h is carried out under thermoneutral conditions ($i = -0.43$ A $cm^{-2}$) at 800 °C in 50 % $H_2O$ + 50 % $H_2$. A low Rp degradation rate (0.162 Ω $cm^2$ $kh^{-1}$) for the investigated cell containing STF fuel electrode is obtained. However, the increasing ohmic resistance during the operational period caused an overpotential increase with a rate of 195 mV $kh^{-1}$. Finally, post-test analyses showed sufficient chemical stability, representing STF as a potential candidate as fuel electrode in SOECs.

## 1. Introduction

Electrolysis is a key technology for the energy transition toward a carbon-neutral energy system. Among the various electrolysis technologies, solid oxide electrolysis cells (SOECs) stand out for their high efficiencies in hydrogen production. Coupled with waste heat, SOECs can exhibit electrical efficiencies exceeding 100 % due to favorable reaction kinetics and thermodynamics resulting from the high operating temperatures, typically between 600 and 900 °C [1–3]. Consequently, integrating SOECs in industry plants with exothermic downstream processes (e.g., production of synthetic fuels, steel, and cement) is desirable [2].

* Corresponding author. Institute of Energy Materials and Devices (IMD-2): Materials Synthesis and Processing, Forschungszentrum Jülich GmbH, 52425, Jülich, Germany.
*E-mail address:* n.h.menzler@fz-juelich.de (N.H. Menzler).

https://doi.org/10.1016/j.jpowsour.2024.236084
Received 30 September 2024; Received in revised form 25 November 2024; Accepted 15 December 2024
Available online 22 December 2024

The challenges with regard to SOEC commercialization are the costs and the long-term service life. The long-term performance of SOECs is affected by the degradation of single-stack components during electrolysis operation. The commonly-used cell materials in SOECs are adapted from solid oxide fuel cells (SOFCs). However, microstructural degradation occurs due to changed operation conditions (e.g., different reactions taking place, different atmospheres, applied voltages) [4]. To address this challenge and achieve the industrial goal of a maximum voltage degradation rate of 0.5 % $kh^{-1}$, currently used SOEC materials must be optimized or new materials investigated [5]. Alternative materials must exhibit high electrochemical performance and excellent chemical stability in long-term SOEC operating conditions.

Besides Ni-GDC (gadolinium-doped ceria), perovskite-based materials are investigated as alternative fuel electrode materials for SOECs. Perovskite oxides have received more and more attention as materials for solid oxide cell (SOC) electrodes due to their suitable properties like high chemical stability, the possession of mixed ionic-electronic conduction, catalytic activity, and good cost-effectiveness [6–9]. In several studies, perovskite-based fuel electrodes based on $(PrBa)_{0.95}(Fe_{0.9}Mo_{0.1})_2O_{5+\delta}$ (PBFM) [10], $Sr_2FeNbO_{6-\delta}$ (SFN) [11] and $Sr_2Fe_{1.5}Mo_{0.5}O_{6-\delta}$ (SFM) double perovskites [12–14], $La_{0.6}Sr_{0.4}Fe_{0.8}Mn_{0.2}O_{3-\delta}$ (LSFM) [15,16], $La_{0.75}Sr_{0.25}Cr_{0.5}Mn_{0.5}O_{3-\delta}$ (LSCM) [17–19] or $SrTi_{1-x}Fe_xO_{3-\delta}$ (STF) [20] were investigated in high-temperature electrolysis operation. Depending on their respective catalytic activity and chemical stability, the new materials were examined under $CO_2$ (e.g., LSFM), steam, or co-electrolysis (e.g., LSFM, LSCM).

$SrTi_{1-x}Fe_xO_{3-\delta}$ is a cubic simple $ABO_3$ perovskite with Sr on the A-site and two elements, Fe and Ti, on the B-site. The properties of the material are strongly related to the respective Fe/Ti ratio. The total conductivity, for example, increases in air with increasing Fe content. At 800 °C, the electronic conductivity $\sigma_{el}$ is 4.5 x $10^{-3}$ S $cm^{-1}$ for x = 0.05, whereas $\sigma_{el}$ increases to 1.8 S $cm^{-1}$ for x = 0.5 [21]. The ionic conductivity follows the same trend and increases with the Fe content. For x = 0.5, $\sigma_{ion}$ is 3.6 x $10^{-2}$ S $cm^{-1}$, which is comparable to the ionic conductivity of YSZ at the same temperature (0.035 S $cm^{-1}$) [22]. Besides higher Fe concentrations, the reduction of $Ti^{4+}$ to $Ti^{3+}$ in hydrogen-rich atmospheres also leads to higher electronic conductivity [23]. The thermal expansion coefficient (TEC) of STF perovskites also increases with increasing Fe content. Zhang et al. [24] presented in their study the increase of the average TEC between 25 and 1000 °C from 12.3 x $10^{-6}$ $K^{-1}$ for x = 0.5 to 27.1 x $10^{-6}$ $K^{-1}$ for x = 0.9. Besides the properties of the pure material, the reactivity of STF with other cell component materials, particularly with the YSZ electrolyte, is being investigated. In general, the formation of secondary phases like $SrZrO_3$ after sintering and also after a heat treatment at 800 °C (SOEC operation temperature) for 150 h, is a common observation [22,25]. Only a few studies on STF-based electrodes for solid oxide cells (SOCs) exist in the literature. Mostly, the material was investigated as fuel electrodes in SOFC operation [22,23], though Zhang et al. [20] examined the properties of STF fuel electrodes in high-temperature steam electrolysis.

They observed a higher sensitivity to steam concentration for STF electrodes with an iron content of less than x = 0.5. Additionally, the trend of decreasing current density with a decreasing Fe content at any given voltage was established in their work. At 800 °C, the authors noticed an increase in the ohmic resistance with decreasing Fe content using an atmosphere of 50 % $H_2O$ + 50 % $H_2$. Fuel electrodes with $SrTi_{0.5}Fe_{0.5}O_{3-\delta}$ stoichiometry exhibited a stable $R_p$ for the increase in steam content from 3 % to 10 %. With steam concentrations higher than 10 %, a slow increase in the polarization resistance from around 0.1 Ω $cm^2$ to 0.15 Ω $cm^2$ for 50 % steam was detected [20].

In this work, a $Sr_{0.98}Ti_{0.5}Fe_{0.5}O_{3-\delta}$ fuel electrode is characterized with regard to its chemical stability and electrochemical properties during electrolysis operation. In particular, we investigated the chemical stability of the pure STF material and the chemical reactivity of the STF with YSZ and GDC under SOEC operating conditions. Additionally, the reactivity of STF with YSZ under manufacturing conditions was examined. Electrochemical characterization of symmetrical cells with STF electrodes and full cells with an STF fuel electrode and an LSCF oxygen electrode was carried out at different steam concentrations and different temperatures. The mid-term degradation behavior of a single cell was then investigated under steam electrolysis conditions at 800 °C up to around 1700 h in 50 % $H_2O$ + 50 % $H_2$. The microstructures of a pristine full cell and of half cells with a NiO/Ni contact layer, heat-treated in SOEC conditions, were analyzed. Lastly, post-test analyses of the electrochemically tested cells were performed.

## 2. Experimental Procedure

### 2.1. Powder preparation

The $Sr_{0.98}Ti_{0.50}Fe_{0.50}O_{3-\delta}$ (STF) perovskite powder was synthesized by the solid-state reaction method. Therefore, stoichiometric amounts of $SrCO_3$ (≥96.5 %, Carl Jäger Tonindustriebedarf GmbH, Germany), $TiO_2$ (≥99 %, Kronos, Germany), and $Fe_2O_3$ (>99 %, Kremer Pigmente GmbH & Co. KG, Germany) were mixed, homogenized for 24 h and then heat-treated in air at 1200 °C for 12 h. The $La_{0.58}Sr_{0.40}Fe_{0.80}Co_{0.20}O_{3-\delta}$ (LSCF) powder was produced in-house using the spray-drying method and a subsequent calcination step which is described more in detail by Serra et al. [26]. The used $Ce_{0.80}Gd_{0.20}O_{1.95}$ (GDC) powder was purchased from Treibacher Industrie AG.

### 2.2. Paste preparation

Screen-printing pastes were prepared by mixing the appropriate amounts of ceramic powder, solvent (Terpineol, DuPont), binder (Ethylcellulose 45/10 cP, Sigma-Aldrich), and further additives (dispersant, pore former). In the case of the STF ink, 47.84 wt% ceramic powder, 47.12 wt% solvent, and 1.04 wt% binder were mixed with 4.00 wt% graphite (TIMREX KS4, Imerys) as pore former and polyvinylpyrrolidone (PVP, Alfa Aesar) as dispersant.

### 2.3. Cell preparation

Electrolyte-supported symmetrical and single cells were fabricated by using commercial 8YSZ electrolyte supports (Kerafol). The support dimensions were 25 × 25 $mm^2$ for the symmetrical cells and 50 × 50 $mm^2$ for the single cells. The support thicknesses were t ≈ 0.15 mm and t ≈ 0.23–0.26 mm for the symmetrical and the single cells, respectively. All the following layers were applied via screen-printing. For both cell types, a GDC barrier layer was added on both sides of the 8YSZ support and sintered at 1300 °C for 3 h. In the next step, the electrodes (area = 10 × 10 $mm^2$) were screen printed. Here, the fuel electrode side (STF) is applied first. After drying the layer at 70 °C for 2 h, STF (symmetrical cells) or lanthanum strontium cobalt ferrite (LSCF) (single cells) layers are applied on the opposite side (oxygen electrode). Afterwards, the electrodes are sintered in two steps. To remove the organics, the electrodes are first heated with 1 K $min^{-1}$ to 750 °C, combined with a holding time of 2 h. Subsequently, the actual sintering temperature of 1050 °C is reached using a heating ramp of 3 K $min^{-1}$. The electrodes are sintered at 1050 °C for 4 h. For the cells measured electrochemically, a NiO contact layer (CL) was applied on top of the STF electrodes of the cells using a brush. Additionally, half cells consisting of YSZ/GDC/STF were prepared similarly. Here, NiO was also applied on top of the STF electrode as a current collector.

### 2.4. Chemical stability and reactivity analysis of STF electrode material

Thermal treatment experiments were carried out to investigate the stability of STF under conditions as similar as possible to those prevailing during SOEC operation of a cell. For stability tests, the pure STF powder and mixtures of STF + 8YSZ (ratio 50:50 wt%) and STF + GDC

(ratio 50:50 wt%) were heat-treated in a 50 % $H_2O$ + 50 % $H_2$ atmosphere at 800 °C for 12 h.

Additionally, the compatibility of STF with YSZ was studied under cell fabrication conditions. For this experiment, STF and 8YSZ powders were mixed in a ratio of 50:50 wt%, and after homogenization, disk-shaped samples with a diameter of 10 mm and a height of 1.5–2 mm were pressed using a uniaxial hand press. The pressed samples were subsequently sintered at 1050 °C for 4 h in air with a heating rate of 3 K $min^{-1}$ and a cooling rate of 5 K $min^{-1}$. Afterwards, the differently heat-treated samples of pure STF and STF mixtures (STF + GDC, STF + YSZ) were analyzed via XRD using a D4 ENDEAVOR diffractometer (Bruker AXS GmbH, Karlsruhe, Germany) with Cu-Kα incident radiation at room temperature. The software HighScore (Malvern Panalytical B.V., Almelo, Netherlands) and Topas V 4.2 (Bruker AXS GmbH, Karlsruhe, Germany) were used for the analysis of the diffraction data and the subsequent Rietveld analyses. The qualitative phase analysis was carried out using the Inorganic Crystal Structure Database (ICSD, FIZ, Karlsruhe, Germany).

### 2.5. Electrochemical measurements

The electrochemical performance of the STF fuel electrodes was investigated by impedance spectroscopy for symmetric and full cells under OCV conditions. IV-characteristics were also measured in fuel cell and electrolyzer mode for the full cell configuration. All tests were performed in a setup described in Ref. [27]. To improve the contact between the STF surface and Ni-mesh current collector and to minimize effects related to the comparably high in-plane resistance of the STF layer, a NiO layer, which is subsequently reduced to metallic nickel during testing, was screen printed on the STF fuel electrodes.

In order to analyze the different loss processes, impedance spectra were recorded in a temperature range from 650 to 800 °C at various hydrogen/steam mixtures. The frequency range was 10 mHz–500 kHz with a voltage amplitude <12 mV. The impedance spectra were analyzed using the distribution of relaxation times (DRT) and a subsequent complex nonlinear least squares (CNLS) fit. In the case of full cells, the air electrode was purged with 375 ml $min^{-1}$ synthetic air (80 % $N_2$ + 20 % $O_2$). After investigating the electrode under different testing conditions, the temperature was kept at 800 °C for 1700 h to study the cell's durability in 50 % $H_2O$ + 50 % $H_2$ at 430 mA $cm^{-2}$. Degradation mechanisms during this period were analyzed by impedance spectroscopy, the impedance of the electrode was measured every 2 h.

### 2.6. Microstructure analysis

The investigated cells were embedded in epoxy resin, ground, and polished along the cross-section to analyze their microstructure. Then, a Cu tape was coiled around each embedded sample to enhance the conductivity, and a thin Pt layer was sputtered on the surface. An SEM (Zeiss Ultra 55/Gemini 450 or Zeiss EVO 15, each with an EDS detector) was used to record electron micrographs. Secondary electron and back-scattered electron detectors were utilized for recording images at acceleration voltages of 8 and 15 kV. The EDS analysis was performed with an acceleration voltage of 20 kV. Besides the pristine and tested full cells, the microstructure of half cells with a NiO contact layer was investigated using a laser microscope (Keyence Color 3D Laser Scanning Microscope VK-9710) and SEM after annealing these for 2 h or 200 h in 50 % $H_2O$ + 50 % $H_2$ at 800 °C.

## 3. Results and discussion

### 3.1. STF phase evolution during processing and operation

One of the aims of the stability experiments was the investigation of the stability of pure STF perovskite material under typical SOEC operating conditions. Therefore, STF powder was heat-treated for 12 h at 800 °C in a 50 % $H_2O$ + 50 % $H_2$ atmosphere, corresponding to averaged (OCV) conditions in an SOEC stack. Afterwards, XRD measurements were carried out, followed by Rietveld refinements of the measured data. References from the inorganic crystal structure database (ICSD) from FIZ Karlsruhe GmbH [28] were used to identify the phases shown in the XRD diffractograms. Fig. 1 displays the Rietveld refinement of the heat-treated pure STF powder and its resulting crystal structure (left).

There is only a small difference between the observed and calculated diffraction patterns of the heat-treated STF powder, leading to the conclusion that the refinement results are plausible. The corresponding crystal structure details of the heat-treated STF and the as-prepared STF, resulting from Rietveld refinements, are summarized in Table 1.

As shown in the diffractogram shown in Fig. 1, only a small amount of an $Fe_3O_4$ secondary phase (ICSD-26410) [29] is formed after 12 h of heat treatment in 50 % $H_2O$ + 50 % $H_2$ at 800 °C. According to the refinement analysis, the largest fraction of the material still consists of the original STF phase (ICSD-92397) [30]. It should be noted that the detection limit of the XRD device is around 4 %. Therefore, the calculated values of 99 % (STF) and 1 % ($Fe_3O_4$) may not be the exact values.

The formation of an $Fe_3O_4$ secondary phase can be explained by an exsolution or particle segregation process of Fe out of the perovskite crystal lattice onto the surface and subsequent oxidation of these particles due to a change in the $pO_2$ during cooling in Ar and sample storage in air before the XRD measurement [31,32]. This could be seen for similar materials/perovskites in several published studies [31–33]. In this study, the results of the conducted SEM analysis did not provide clear evidence of exsolved Fe particles (see Fig. S9 in the supplementary material). A comparison of the as-prepared STF powder to the heat-treated STF shows no change in the Pm-3m (227) space group of the material but a slight change in the lattice parameters and therefore, in the cell volume. The lattice parameter, ***a***, increases on a small scale after exposure to the tested operating conditions from 3.896 Å for the starting powder to 3.910 Å. As a result, the crystal lattice volume changes from 59.14 $Å^3$ to 59.80 $Å^3$, indicating a minor volume increase of around 1.12 % for the heat-treated STF. This slight volume expansion could be attributed to a reduction of the average oxidation state of the B-site atoms (Ti, Fe) connected with an increasing oxygen loss during the exposure to operating SOEC fuel electrode conditions [34–36].

In addition to the experiments for the pure perovskite powder, mixtures of STF with GDC and YSZ were heat treated under the same simulated SOEC operating conditions (800 °C in 50 % $H_2O$ + 50 % $H_2$, 12 h). The ratio between the perovskite and GDC or YSZ is 50:50 wt%. The resulting diffractograms from the XRD measurements of STF + YSZ and STF + GDC can be found in Fig. 2 a). The XRD pattern of the STF + YSZ mixture clearly shows the formation of $Fe_3O_4$ (ICSD-26410) and $SrZrO_3$ (ICSD-89365) [37] secondary phases during annealing at 800 °C in 50 % $H_2O$ + 50 % $H_2$. According to the corresponding Rietveld analysis, the heat-treated STF + YSZ powder mixture contains ca. 47 % of the STF phase (ICSD-92397), around 43 % of the YSZ (ICSD-75316) [38] phase and smaller amounts of $SrZrO_3$ and $Fe_3O_4$ phases with 8 % and 2 %, respectively. A possible explanation for the occurrence of the $Fe_3O_4$ phase is already given in the section above regarding the stability of the pure perovskite material. Many publications have already observed the formation of an ion-blocking $SrZrO_3$ phase for mixtures of perovskites and YSZ in solid oxide cell operation and SOC manufacturing [22,39,40]. The segregation of Sr ions leads to the formation of a $SrZrO_3$ phase, which causes a performance loss during cell operation [40,41]. In general, the XRD results in this study show a strong interaction between STF and YSZ during the heat treatment at 800 °C for 12 h under a corresponding oxygen partial pressure of $pO_2 = 4.4 \times 10^{-19}$ atm.

In order to prevent the interaction and in particular the formation of the $SrZrO_3$ phase during the manufacturing or operation of solid oxide cells, a barrier layer is usually applied. In the case of perovskite electrodes combined with stabilized zirconia electrolytes, the barrier layer is typically composed of GDC. The good compatibility between STF and

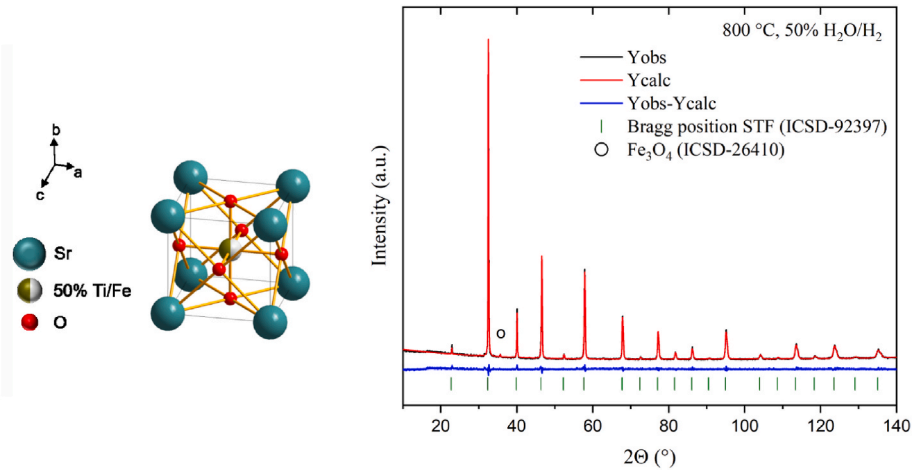


**Fig. 1.** Crystal structure (left) and Rietveld refinement (right) of the 12 h heat-treated STF @800 °C in 50 % $H_2O$ + 50 % $H_2$.

**Table 1**
Structural details of the STF perovskite before and after thermal treatment.

| Sample | | STF | Heat-treated STF (800 °C, 50 % $H_2O$ + 50 % $H_2$) | |
|---|---|---|---|---|
| Phase | | $Sr_{0.98}Ti_{0.5}Fe_{0.5}O_{3-\delta}$ | $Sr_{0.98}Ti_{0.5}Fe_{0.5}O_{3-\delta}$ | $Fe_3O_4$ |
| Quantity [wt.%] | | 100 | 99 | 1 |
| Space group | | Pm-3m (221) | Pm-3m (221) | Fd-3m (227) |
| Lattice parameters | a [Å] | 3.896 | 3.910 | 8.3941 |
| | b [Å] | 3.896 | 3.910 | 8.3941 |
| | c [Å] | 3.896 | 3.910 | 8.3941 |
| | V [Å$^3$] | 59.14 | 59.80 | 591.46 |
| | α [°] | 90.0000 | 90.0000 | 90.0000 |
| | β [°] | 90.0000 | 90.0000 | 90.0000 |
| | γ [°] | 90.0000 | 90.0000 | 90.0000 |

Gd/Sc doped ceria is already shown in several [42,43] and can be confirmed by the results from this study. In contrast to YSZ, GDC demonstrates good chemical compatibility with the STF perovskite under the tested conditions in this study, see Fig. 2 (a).

In the diffractogram of the STF + GDC mixture after the experiment in Fig. 2 a), no interaction between the two materials can be observed during the 12 h test duration. Every peak in the diffraction pattern of the mixture after the heat treatment can be attributed to either the STF (ICSD-92397) or the GDC phase (ICSD-251477) [44].

The chemical reactions between STF and 8YSZ during the electrolyte-supported cell preparation process were also examined. For this purpose, STF and 8YSZ powder mixtures, with a ratio of 1:1 wt%, were prepared and sintered at 1050 °C for 4 h, following the sintering regime used in this study for the electrolyte-supported cells. The result of the XRD analysis is shown in Fig. 2 b). The diagram clearly illustrates secondary phase formation and phase changes after the sintering of the powder mixture. The formation of secondary phases after sintering mixtures of YSZ and perovskites with high Sr-activity was expected, as already described in several publications [22,39,45].

A Rietveld refinement confirmed secondary phases of $SrZrO_3$ (ICSD-89365) and $SrFe_{12}O_{19}$ (ICSD-66403) [46] as well as two existing types of STF perovskite phase with differences in their lattice parameter ***a***. One STF phase featured a calculated lattice parameter of ***a*** = 3.930 Å. The other STF phase has a comparably smaller lattice parameter of 3.902 Å. According to Molin et al. [22], the possible integration of Zr into the STF lattice and $SrZrO_3$ formation, which potentially replaces Fe and/or Ti on the B-site, could result in a change in the perovskite's lattice parameters. Their study stated that starting from sintering temperatures of 1000 °C, $SrZrO_3$ is formed for the STF + YSZ mixtures [22].

$SrFe_{12}O_{19}$ secondary phases in perovskites are typically found during the synthesis of perovskites before reaching their single-phase final state [47]. Schulze-Küppers et al. [34] discovered that heat treatment of STF below 950 °C showed $SrFe_{12}O_{19}$ alongside orthorhombic and cubic perovskite structures. Only with a temperature above 1100 °C, a single cubic STF phase could be obtained. In this study, the material was synthesized via the solid-state reaction method, while in Ref. [34] a modified Pechini route was used to prepare the STF. Therefore, differences in the phase transitions and secondary phase formation temperatures could originate from the respective synthesis method. Since for

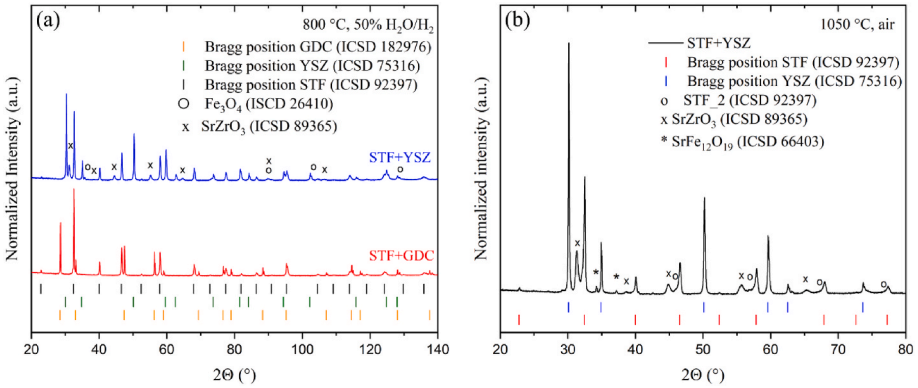


**Fig. 2.** XRD patterns of powder mixtures (1:1) for a) STF + YSZ and STF + GDC heat-treated at 800 °C in 50 % $H_2O$ + 50 % $H_2$ for 12 h and b) STF + YSZ sintered at 1050 °C in air for 4 h.

the Pechini method lower calcination temperatures can be applied to obtain a pure cubic perovskite phase compared with the solid-state route [48,49], phase transitions and secondary phase appearances and disappearances are to be expected at rather higher temperatures for the material used in this study.

### 3.2. Electrochemical performance

The overview of obtained polarization resistance ($R_p$) and ohmic resistance ($R_\Omega$) for the tested cells with $Sr_{0.98}Ti_{0.5}Fe_{0.5}O_3$ (STF) fuel electrodes in the temperature range of 650–800 °C are shown in Table 2. The resistance values are extracted from fitting an equivalent circuit model (ECM) consisting of a series resistance $R_\Omega$ and serial $R_nQ_n$ elements to the impedance spectra. The electrochemical performance is investigated in symmetrical and full-cell configurations to examine the electrochemical processes involved in hydrogen oxidation/evolution and their degradation for the developed fuel electrode material. The results for the symmetrical cell show a high electrocatalytic activity of the investigated cell toward steam electrolysis. The concentration of steam also appeared to have an impact on electrochemical performance. Accordingly, the polarization resistance decreases with steam concentration in the range of 3 %–20 % $H_2O/H_2$ and increases again above 20 % $H_2O/H_2$. The minimum value $R_p = 0.050\ \Omega\ cm^2$ is obtained at 800 °C using 20 % $H_2O/H_2$. The significant increase in polarization resistance might be related to the deactivation of the electrode surface or the decreasing number of oxygen vacancies in STF perovskite originating from the increasing oxidation state of the cations [12,13]. Accordingly, the polarization resistance in 90 % $H_2O/H_2$ increases to $0.255\ \Omega\ cm^2$ at 800 °C, about four times higher than the mean value in the steam range of 3–20 %. Similar behavior was also observed for the ohmic resistance while increasing the oxygen partial pressure. This is most likely due to changing the valence state of the cations in the STF perovskite at high steam concentrations, reducing the electronic and ionic conductivity of STF [23]. The rising ohmic resistance can also be caused by the GDC-interdiffusion layer at the GDC/YSZ interface, where increasing the $pO_2$ decreases its conductivity [50].

After providing an overview of the ohmic and polarization resistances of the STF fuel electrode, we will analyze the impedance spectra and discuss the impact of the operation conditions using fitting an appropriate ECM. The Nyquist plot and corresponding distribution of relaxation times (DRT) in 3 % $H_2O/H_2$ at the temperature range of 650–800 °C are illustrated in Fig. 3. Note that the impedance spectra correspond to the polarization resistance of two STF electrodes in a symmetrical cell configuration and must be divided by two for one electrode.

The impedance spectra were analyzed using in-house software to identify the processes contributing to the overall cell performance. DRT can deconvolute electrochemical reactions as well as migrative and diffusive transport processes with close time constants for better understanding [51]. The DRT calculation is a complex process that involves several input values, including the frequency range, the number of impedance values, the regularization parameter (λ), and the number of points per decade (τ). The regularization parameter is the most crucial factor in the DRT calculation, as it smooths the profile and prevents artificial peaks [52]. By selecting an optimal value of $\lambda = 0.01$, a constant number of 4 individual peaks with different relaxation frequencies could be identified in all measured impedance spectra.

Accordingly, the overall impedance spectra of the STF electrode in steam electrolysis show four peaks in the DRT: one high-frequency peak (HF, $f > 10^4$ Hz), two middle-frequency peaks (MF, $f = 10–10^4$ Hz), and one low-frequency peak (LF, $f < 10$ Hz). By identifying these peaks in the DRT of the STF electrode, the following equivalent circuit is considered to study the electrochemistry of the fuel side of prepared solid oxide cells using a mixture of steam and hydrogen gases.

$$R_\Omega(R_1Q_1)(R_2Q_2)(R_3Q_3)(R_4Q_4) \quad (1)$$

The complexity of electrochemical processes makes it challenging to interpret physicochemical backgrounds. They are affected by steam concentration, cell processing techniques, microstructure variations, chemical composition, and surface chemistry of the mixed ionic and electronic conductor (MIEC) electrode [53]. A more detailed analysis can be done with the coupling of transport processes and charge transfer reactions using a transmission line model (TLM) [54]. However, using complex TLM approaches requires pre-parameterizing the physical and microstructural properties of electrodes by extensive electrical, electrochemical, and microstructural characterization, which is far beyond the scope of this article. Thus, the simplified ECM (Eq. (1)) is applied here, assuming that a single loss process in the STF-fuel electrode dominates each of the 4 peaks in the DRT.

Temperature and partial pressures of gases are the most commonly used parameters for determining the characteristic features of the processes in SOCs [12,13,53]. Varying those operating parameters provides information about the physicochemical background of the peaks in the DRT [55]. Following this, Fig. 3c and d provide the dependencies of the polarization resistances on temperature and steam partial pressure, respectively.

**Table 2**
Overview of ohmic resistance (RΩ) and polarization resistance (Rp) for the tested STF fuel electrode at the temperature range of 650–800 °C and in different steam concentrations for (a) symmetrical cell configuration, and (b) full cell configuratio concentrations for (a) symmetrical cell configuration, and (b) full cell configuration, containing LSCF air electrode. Note: Rp and RΩ values for the symmetrical cell are for one STF fuel electrode, and in the case of the full cell, are for the STF and LSCF electrodes.

| Cell configuration | Temp. (°C) | Resistance (Ω cm²) | Steam concentration in hydrogen (x% $H_2O$ in $H_2$) | | | | | |
|---|---|---|---|---|---|---|---|---|
| | | | 3 % | 10 % | 20 % | 50 % | 70 % | 90 % |
| Symmetric cell | 650 | $R_\Omega$ | 2.553 | 3.695 | 3.572 | 3.486 | 4.840 | 5.624 |
| | | $R_p$ | 0.508 | 0.694 | 0.642 | 0.747 | 1.428 | 2.350 |
| | 700 | $R_\Omega$ | 1.376 | 2.037 | 1.920 | 2.003 | 2.817 | 3.323 |
| | | $R_p$ | 0.196 | 0.223 | 0.226 | 0.304 | 0.603 | 1.014 |
| | 750 | $R_\Omega$ | 0.785 | 1.125 | 1.048 | 1.203 | 1.686 | 2.062 |
| | | $R_p$ | 0.097 | 0.096 | 0.100 | 0.145 | 0.279 | 0.467 |
| | 800 | $R_\Omega$ | 0.489 | 0.666 | 0.623 | 0.765 | 1.062 | 1.304 |
| | | $R_p$ | 0.068 | 0.053 | 0.050 | 0.078 | 0.144 | 0.255 |
| Full cell | 650 | $R_\Omega$ | 2.741 | 2.966 | 3.013 | 3.112 | 3.287 | – |
| | | $R_p$ | 0.682 | 0.721 | 0.718 | 0.855 | 1.137 | – |
| | 700 | $R_\Omega$ | 1.627 | 1.706 | 1.713 | 1.813 | 1.930 | – |
| | | $R_p$ | 0.276 | 0.267 | 0.268 | 0.359 | 0.488 | – |
| | 750 | $R_\Omega$ | 1.002 | 1.025 | 1.027 | 1.094 | 1.189 | – |
| | | $R_p$ | 0.132 | 0.121 | 0.127 | 0.177 | 0.233 | – |
| | 800 | $R_\Omega$ | 0.655 | 0.671 | 0.668 | 0.718 | 0.779 | – |
| | | $R_p$ | 0.085 | 0.066 | 0.068 | 0.092 | 0.129 | – |

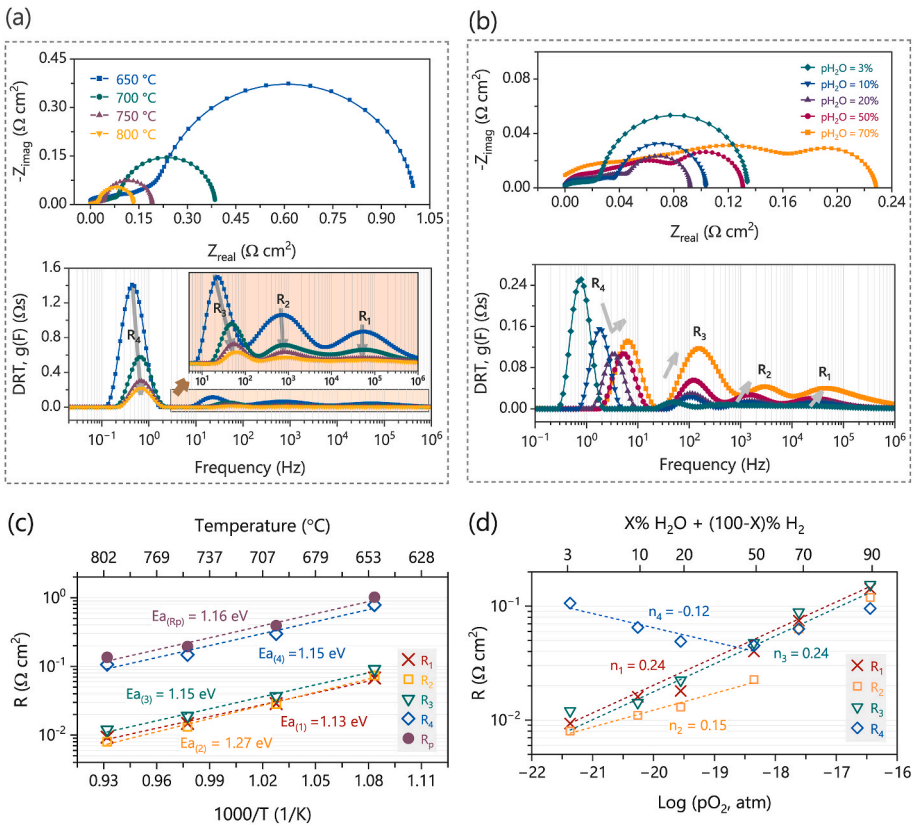


**Fig. 3.** (a) Temperature and (b) concentration dependency of the Nyquist spectra corresponding DRT plots, (c) Arrhenius plots of fitted polarization resistance contributions in 3 % $H_2O$ + 97 % $H_2$ fuel, and (d) steam concentration dependency of polarization resistance contributions at 800 °C. Note: the polarization resistance is measured for two electrodes in a symmetrical cell configuration.

The fitting resistance in Fig. 3d shows that the low-frequency process (LF-$R_4$) mainly limits the cell performance in 3 % $H_2O$ + 97 % $H_2$, covering 77 ± 1 % of the polarization resistance, while the fitted resistances are at the same order of magnitude with operation in 50 % $H_2O$ + 50 % $H_2$ atmosphere. It is necessary to mention that the close relaxation frequency of the process in the DRT plot can increase calculation error for the thermal activation energies (Ea) and reaction orders (n). The DRT plots (Fig. 3b) and calculated activation energy (Fig. 3c) show a thermally activated process for all fitted resistances. Based on this finding, none of the 4 processes is solely related to gas diffusion, as it is not thermally activated. The apparent Ea for the HF-$R_1$ process is 1.13 eV, and similarly high Ea values are calculated for the MF-$R_2$-$R_3$ (1.21 ± 0.06 eV) and LF-$R_4$ (1.15 eV) processes. This high Ea value for the STF electrode matches a former study on (Sr, Ti)$O_3$-based perovskite [56]. It represents the operation requirement above 750 °C to achieve sufficient electrocatalytic activity toward hydrogen evolution/oxidation and high electronic and ionic conductivity to minimize the cell overpotential.

The relationship between polarization resistance and steam concentration, consequently related to oxygen partial pressure, $pO_2$, leads to the reaction order (n) through the $R = k(pO_2)^{-n}$ equation [57]. Here, the equilibrium $pO_2$, resulting from the $H_2O/H_2$-ratio and temperature, impacts the electrochemical properties of the subjected STF perovskite electrode that mainly depend on the gas species activity. This approach is feasible for electrochemical reactions at the MIEC electrode surface (charge transfer and other surface chemistry-related processes) and changing electrode conductivity based on defect chemistry at specific $pO_2$. In general, the n-value provides information about the type of species involved in electrochemical reactions and the defect chemistry of the electrode material. The HF-$R_1$ process shows a concentration dependency of 0.24 in this work, and n for the MF-$R_2$ and MF-$R_3$ processes is calculated in the range of 0.15–0.24, while the reaction kinetics accelerate in the LF-$R_4$ process with a negative reaction order of −0.12. It must be highlighted that the fitted resistance for the $R_4$ and $R_2$ processes no longer follow the linear behavior when the steam concentration increased above 50 % $H_2O$ + 50 % $H_2$. This means that the fuel composition highly influences the characteristics of STF perovskite electrode during testing and most probably changes the rate determining reaction step in this $pH_2O$ range. Similar behavior has also been reported for other MIEC electrode materials [12,58].

The deviation from linear behavior may be caused by an increasing number of oxidation states of the cations and a decrease in oxygen vacancies in the STF perovskite at high steam concentrations, thereby increasing resistance at MF and LF due to decreasing active sites on the electrode surface [59]. Moreover, overlapping different physicochemical processes, especially low-frequency gas diffusion resistance in high steam concentrations (i.e., 70 % and 90 % $H_2O$ in $H_2$), might also cause the reaction order to deviate from linear behavior.

The $R_1$ in the high-frequency regions with a reaction order of 0.24 and high activation energy represents the characteristic features of a charge transfer or transport process at a solid/solid interface [60]. The calculated capacitance ($10^{-4}$-$10^{-3}$ F $cm^{-2}$) is in the capacitance range for double layers [61]. In other words, HF-$R_1$ reflects an interfacial process, in our case, either the STF/GDC interface or the GDC/YSZ interface [13]. It should be mentioned that the charge transfer process remains one of the least understood aspects of electrochemistry for MIEC materials, even though numerous studies have been conducted on this process [52]. Besides, such charge transport/charge transfer processes at the GDC/YSZ interface are strongly affected by insulating zirconate interlayers [62], and even minor changes in material and processing can result in significant variations of the related resistances [63].

The contribution of the Ni contact layer on cell performance should also be discussed before interpreting electrochemical reactions at the MF

and LF ranges. The SEM images in the post-mortem analysis illustrated that the high mobility of Ni particles during the cell operation could influence the contribution of the applied Ni contact layer due to the coverage of the STF surfaces with Ni nanoparticles. This phenomenon could increase the electrocatalytic activity of the STF surface, similar to Ni-exsolution compounds [64] and nanoparticles generated by infiltration [65].

To determine the contribution of the Ni contact layer in the electrochemical performance, in addition to investigated cells, the Ni contact layer is replaced with an Au contact layer and tested in 3 % $H_2O$ + 97 % $H_2$ at 800 °C. The results demonstrated an 18 % increase in the polarization resistance from 0.085 to 0.10 Ω $cm^2$ (Fig. S1), with a higher contribution of HF resistance to the Rp. The increase in Rp for recorded impedance spectra at this initial testing stage is mainly due to the low sinterability of the Au contact layer in comparison to the NiO layer at 800 °C. Moreover, the high degradation rate of Au contact paste caused a high degradation rate in ohmic resistance, hindering the reasonability of performing a long-term performance study. Anyhow, based on this finding, it can be concluded that the Ni-contact layer does not determine the STF electrode performance.

The fitted MH-$R_3$ represents a high activation energy (Ea = 1.15 eV) and reaction order (n = 0.24). The coupling of surface reactions with oxide ion transportation is a well-known phenomenon for MIEC electrodes at the air side of solid oxide fuel cells [55,66,67]. This process can be assumed to originate from the $O^{2-}$ transportation resistance in the STF electrode coupled with the dissociative adsorption of steam molecules on the STF surface.

The LF-$R_4$ process with an apparent activation energy of 1.15 eV shows a negative reaction order (n = −0.12) at a steam concentration range of 3–50 % $H_2O/H_2$. The polarization resistance at low frequency decreases with steam concentrations and increases above 50 % $H_2O$ + 50 % $H_2$. While gas diffusion/conversion processes are often observed at low frequencies, these can be ruled out due to the high apparent activation energy of $R_4$ [68,69]. Notably, the characteristic frequency of $R_4$ is very sensitive to the steam concentration in the fuel gas and increases with increasing $pH_2O$. A dominant impedance response at low frequencies has been observed for STF and related materials, and attributed to the oxygen exchange reaction on the perovskite surface [42,70].

The corresponding capacitance value of 1.77 F $cm^{-2}$ demonstrates that the LF-$R_4$ is related to non-charge transfer processes like solid-state transport or oxygen surface exchange [71]. The improvements in surface reaction with steam concentration are compatible with those reported for MIEC electrodes before [72,73], and the oxygen incorporation/release reaction on the electrode surface would also give rise to a large chemical capacitance [74]. Therefore, the LF-$R_4$ process is most likely related to a surface reaction on the STF electrode due to the incorporation/release of oxygen into the perovskite structure.

Similar to the STF symmetrical cell, the electrochemical performance of the STF electrode is measured in a full-cell configuration. It must be mentioned that using 90 % $H_2O$ + 10 % $H_2$ gas appeared to have permanent degeneration on $R_\Omega$ and Rp due to the contact issue between the STF electrode and Ni current collector layer, affecting the following sequence of long-term electrochemical study. For this reason, we have excluded measuring polarization resistance in 90 % $H_2O$ + 10 % $H_2$ for full cell configuration.

The Nyquist plot and the corresponding distribution of relaxation times (DRT) in 3 % $H_2O/H_2$ at the temperature range of 650–800 °C, are provided in Fig. 4. The DRT plots represent an additional peak (R′) at the frequency range of $10^2$–$10^3$ Hz, identifying five processes contributing to the total polarization resistance for steam electrolysis (Fig. 4 b). According to the fit, the corresponding resistance at 650 °C is estimated at 0.140 Ω $cm^2$, using 50 % $H_2O$ + 50 % $H_2$ on the fuel side and synthetic air on the air side. Increasing temperature at the same gas compositions significantly reduces R' to 0.010 Ω $cm^2$, whereas the activation energy

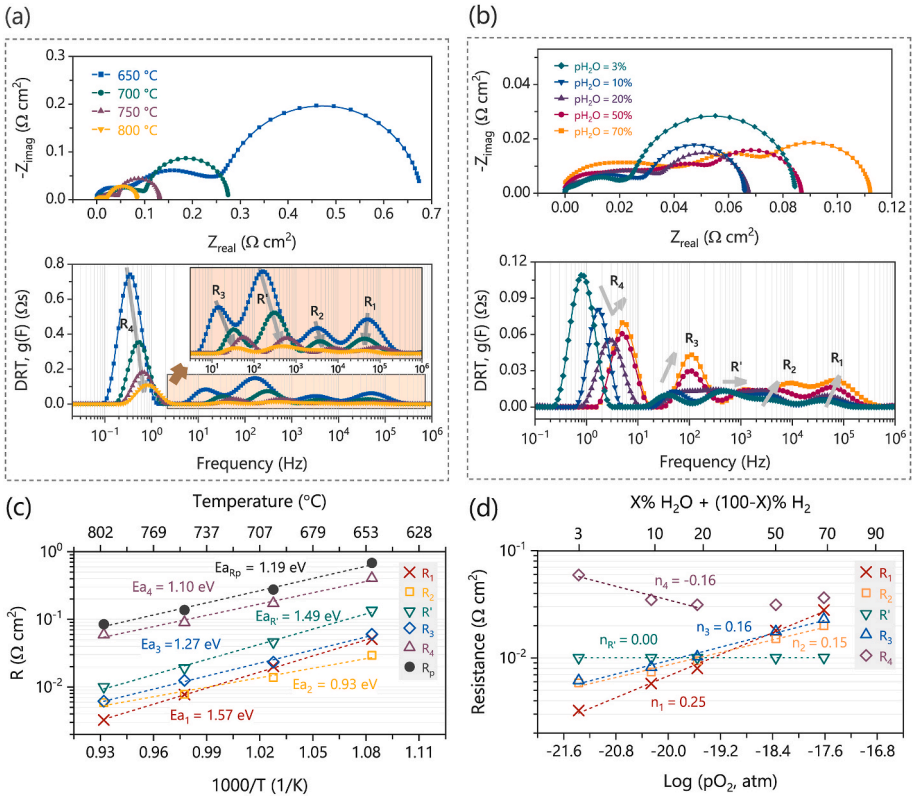


**Fig. 4.** (a) Temperature and (b) concentration dependency of the Nyquist spectra corresponding DRT plots, (c) Arrhenius plots of fitted resistances for tested cell in 3 % $H_2O$ + 97 % $H_2$ fuel, and (d) steam concentration dependency of sub-polarization resistances for the STF electrode in full-cell configuration tested at 800 °C. Note: In (d) the steam to hydrogen ratio is varied whereas the $pO_2$ at the air electrode is kept constant at 0.21 atm, thus R' is attributed to the air electrode is not affected.

for this resistance is calculated at 1.49 eV (Fig. 4 c). This is in excellent agreement with the investigations on other cells exhibiting the same LSCF air electrode [69].

By varying the steam concentration supplied to the fuel side, only the STF electrode impedance processes should be affected, and the air electrode resistance is expected to be unaffected. The dependency of polarization resistance on the steam concentration ($pO_2$), while using synthetic air on the air side, illustrates that the R′ resistance stays almost constant $R_3 = 0.010 \pm 0.001\ \Omega\ cm^2$ with reaction order of n = 0.00 (Fig. 4d). It reveals that the R' at the MF range is most likely related to oxygen reduction reaction (ORR) in the LSCF perovskite. The perovskite air electrode operating at high-temperature steam electrolysis also exhibits a corresponding resistance at $10^2$–$10^3$ Hz, as shown in the previous study [57,75]. [76].

It should be noted that the air electrode, respectively the SZO layer between GDC and YSZ on the air side, also contributes to the high-frequency processes in the range of HF-$R_1$ [77]. Nevertheless, the same origin and relaxation frequency make it difficult to distinguish the contributions of the STF-fuel and LSFC-air electrodes.

After identifying the processes in steam electrolysis on the STF electrode, the durability study of the prepared electrode was carried out for 1700 h under initially thermoneutral conditions ($I = -0.43\ A\ cm^{-2}$) at 800 °C using 50 % $H_2O$ + 50 % $H_2$ on the fuel side and synthetic air on the air side for steam electrolysis. Accordingly, the Ni|STF|GDC|YSZ|GDC|LSCF full cell was operated under a galvanostatic test, and impedance spectra were measured under current and OCV conditions every 2 h. Since the reaction kinetic highly changes under applied current, the impedance spectra measured under OCV conditions are considered for evaluating the degradation mechanisms during the durability study to have a reasonable comparison with the identified processes above.

The overview of the variation of $R_\Omega$, $R_p$, and overpotential is shown in Fig. 5. According to the obtained results, a relatively fast degradation rate is observed in the first 150 h of testing. At this stage, the degradation rate for $R_p$ and overpotential have been recorded at about $0.404\ \Omega\ cm^2$ and 490 mV $kh^{-1}$, respectively. As the aging time increases, linear behavior is observed, with a decreasing degradation rate. Accordingly, the degradation rate for $R_p$ and overpotential decreased to $0.162\ \Omega\ cm^2$ and 195 mV $kh^{-1}$, respectively. The durability study demonstrates that the degradation of electrochemical performance is mainly due to increasing ohmic resistance in the cell.

The transformation of cubic 8YSZ (C-YSZ) to tetragonal 8YSZ (T-YSZ) is the phenomenon reported to occur while the SOCs operate over a long-term period [78,79]. Although forming a tetragonal phase can improve the mechanical properties, it negatively affects the 8YSZ electrolyte conductivity [78,80]. Accordingly, depending on the operation condition, the 8YSZ conductivity can drop to 50–80 % of the initial value due to forming a tetragonal phase with lower ionic conductivity and consequently increasing the ohmic resistance of the cell [79,81].

In addition, developing the $SrZrO_3$ (SZO) caused by the segregation of Sr cations to the LSCF surface and diffusion toward the electrolyte adversely affects electrochemical performance by increasing the cell resistances [52,66]. The accumulation of the SZO insulating phase at the electrolyte/air electrode interface not only blocks the migration of oxygen ions at this interface but also deteriorates the electrocatalytic activity and electrical conductivity of LSCF electrodes due to a significant Sr deficiency in the A-site of the perovskite structure [82–84]. Following the two phenomena mentioned above, the postmortem microscopy analysis shows that the SZO insulating phase forms extensively at the GDC/YSZ interface (Fig. S4).

The variation of DRT with operating time was implemented to discuss degradation mechanisms for polarization resistance. Fig. 6 shows the DRT plots of the electrochemical impedance spectra measured during the galvanostatic durability test. Similar to the initial impedance obtained for the STF full-cell, five distinguishable peaks are observed. All the processes show increasing resistance during the durability test. A substantial shift of the relaxation frequency was observed for MF-$R_3$ and LF-$R_4$ processes, and the DRT peak for LF-$R_4$ showed a fast increase over the first 450 h, and then a lower degradation rate was recorded until 1700 h. The degradation of LF-$R_4$ and MF-$R_3$ is mainly due to STF electrode properties, in which increasing the LF-$R_4$ resistance could be due to the changing surface chemistry causing a decrease in the electrode kinetics for the oxygen incorporation/release reaction. The coupling of surface exchange and $O^{2-}$ transport at the STF-surface and the STF-bulk explains the increase and relaxation frequency shift in MF-$R_3$ resistance.

The DRT peak for the MF process shows that the $R_2$ is less severely affected during the investigated period. However, the R′ process slightly degrades, corresponding to the oxygen reduction reaction on the LSCF air side. The important degradation mechanism in the LSCF electrode is the segregation of Sr cations onto the electrode surface, forming non-electrocatalytically active SrO phases. Hence, increasing the R' resistance is most probably due to the surface deactivation of the LSCF electrode from the air side [57,85,86].

The HF-$R_1$ process is the second process that has a reasonable impact on polarization resistance. Increasing corresponding resistance could originate from two phenomena: (i) formation of insulating SZO phase at the electrode/electrolyte interface, and (ii) degradation of YSZ electrolyte with transforming the C-YSZ to T-YSZ phase.

Overall, analysis of the degradation behavior using the impedance spectra demonstrates that the electrochemical performance of the investigated cell is limited mainly due to the high degradation rate of ohmic resistance. The average voltage degradation of around 14 % $kh^{-1}$ is significantly higher than the industrial goal of 0.5 % $kh^{-1}$ and needs to be improved.

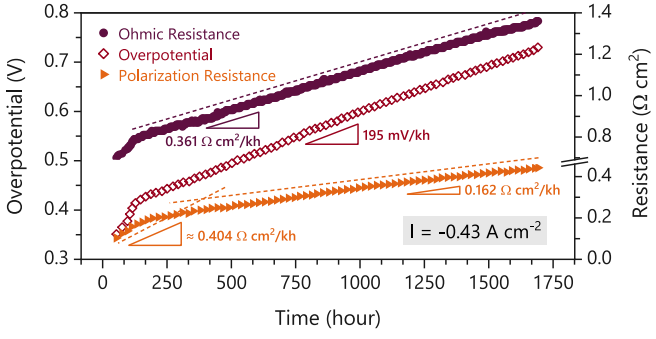


**Fig. 5.** Overview of performance degradation for the STF|8YSZ|LSCF cell over 1700 h in 50 % $H_2O$ + 50 % $H_2$ fuel at 800 °C. Note: the impedance spectra are under OCV condition, and chronoamperometry is recorded at the thermoneutral condition at 800 °C with a constant current of $-0.43\ A\ cm^{-2}$.

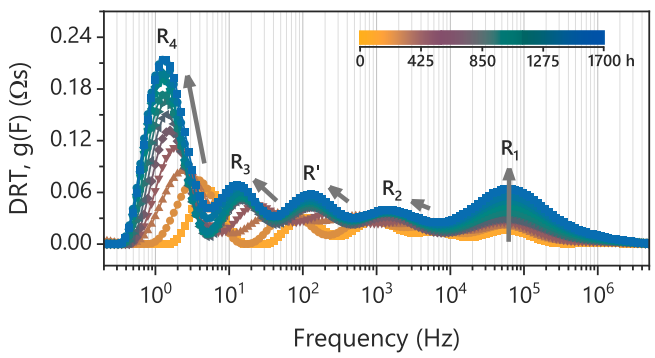


**Fig. 6.** The DRT plots of the electrochemical impedance spectra measured under thermoneutral conditions ($I = -0.43\ A\ cm^{-2}$) at 800 °C using 50 % $H_2O$ + 50 % $H_2$ for 1700 h.

### 3.3. Post-test analysis

After the mid-term stability test under $H_2O$ electrolysis operation up to around 1700 h, the tested full cell was embedded and polished along the cross-section. A full cell in the as-prepared state was also embedded to provide a reference. Afterwards, both cells were characterized via SEM and EDS analysis.

The microstructure and elemental mapping analysis shown focuses on the STF electrode, the STF/GDC barrier layer interface and the GDC/8YSZ electrolyte interface. The results of the conducted SEM and EDS analyses of the oxygen electrode side are summarized below, the corresponding images can be found in the supplementary file.

The overview of the LSCF oxygen electrode, GDC barrier layer and 8YSZ electrolyte for the cell before and after the 1700 h operation is shown in Fig. S2. The images show no obvious change in the microstructure after the SOEC operation. There are no cracks or delamination processes detectable. Reasons for the different layer thicknesses for the cell before and after the operation will be discussed later in the section about the fuel electrode. A comparison of the EDS analyses of the as-prepared (Fig. S3) and the tested cell (Fig. S4) indicates the presence of SZO secondary phases at the GDC/8YSZ interface for both cells. Consequently, it can be concluded that at least a large part of the SZO phase was formed during the manufacturing process. This was also observed in other publications in the case of a porous GDC barrier layer [87–90], as is also the situation in this study. Based on the SEM images, a slight increase in the SZO phase fraction but no continuous strontium zirconate layer formation at the GDC/8YSZ interface can be ascertained. The formation of the SZO phase during the electrolysis operation would usually result in a performance loss over time with increasing secondary phase, as already mentioned in section 3.2. Since forming the SZO can be observed right after sintering and no continuous SZO phase can be detected at the GDC/8YSZ interface after SOEC operation, the largest share of the degradation of the ohmic resistance can be attributed to other reasons. Nevertheless, the increase of the SZO phase during operation and its possible influence on the performance must be investigated further. Furthermore, Co segregation in one area near the GDC/LSCF interface could be observed after the electrolysis operation. This was also seen for LSCF electrodes in other studies after electrochemical polarization [4,90,91]. According to Unachukwu et al. [90], the formation of cobalt oxide particles and the segregation of Sr could cause degradation of the LSCF electrode. However, as only a small amount of Co-rich phase was found in this work, a significant influence of Co segregation on the degradation of LSCF is questionable.

Fig. 7 shows an overview of the STF fuel electrode, GDC barrier layer, and 8YSZ electrolyte for the as-prepared full cell (a) and the tested full cell (c). No significant changes are observed in the STF fuel electrode, the STF/GDC interface or the GDC/8YSZ interface before and after the mid-term degradation test. The overall microstructure of the STF fuel electrode and the GDC layer of both cells is very similar.

There seems to be good adhesion between the STF fuel electrode and the GDC barrier before and after the stability test. Moreover, both cells show a homogeneous GDC barrier layer of 5–7 μm thickness. A difference between the images of the as-prepared and the 1700 h tested full cell is observed in the fuel electrode thickness. The fuel electrode of the as-prepared full cell is with 35–36 μm thicker compared to the value of ca. 30–31 μm of the tested cell. Several possible explanations exist for the observed layer difference before and after the electrochemical test. First, the semi-automatic screen-printing method, applied during the cell preparation, can sometimes lead to a layer distribution that is not completely homogeneous. As a result, the samples may show minor differences in layer thickness depending on the cell area from which the respective sample was taken. As the penetration depth in MIEC electrodes is usually less than 20 μm, the observed thickness variation should not affect the performance. Also, applying a contact layer on top of the STF electrode combined with the experimental setup could lead to a ripping of parts of the STF fuel electrode while demounting the cell after the measurement. Fig. 7 (b) and (d) show the STF fuel electrode, the STF/GDC interface, and the GDC/8YSZ interface of the as-prepared and 1700 h tested full cell in more detail. This closer look confirms the good adhesion between the STF fuel electrode and the GDC in both cells. However, in Fig. 7 (d) changes in the form of cracks and fractures are visible after 1700 h of operation. Compared to only a small number of cracks at the STF/GDC interface, a considerable number of cracks can be found inside the GDC layer and at the GDC/YSZ interface. This observation is in line with the known chemical expansion of GDC in reducing atmospheres [92,93]. These cracks and fractures could influence the

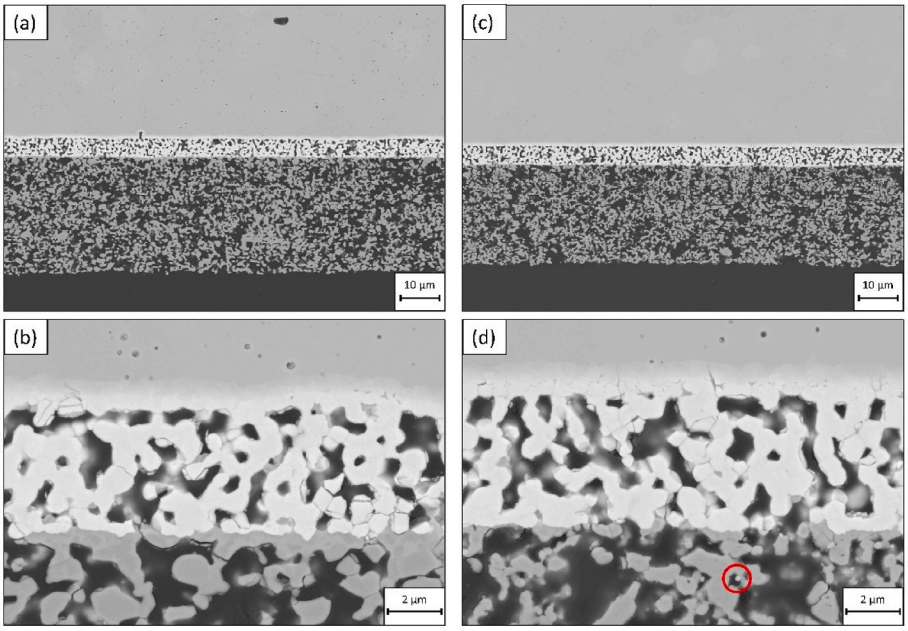


**Fig. 7.** Backscattered electron (BSE) images of the STF fuel electrode, GDC and YSZ cell layers of a) and b) the overview and the STF/GDC/YSZ interface in more detail of a sintered (air, 1400 °C), pristine full cell and c) and d) the overview and the STF/GDC/YSZ interface in more detail of the full cell tested in electrolysis mode (800 °C, 50 % $H_2O$ + 50 % $H_2$, i = −0.43 $Acm^{-2}$) after ca. 1700 h; grown particle marked by circle in (d).

degradation/performance behavior of the cell during the electrochemical testing.

Furthermore, grown and (comparatively) spherical particles can be observed in the tested cell. These particles can be seen predominantly in the STF fuel electrode, and the GDC layer. Besides the SEM images, EDS analyses of full cells before and after the mid-term degradation test were carried out. Elemental mappings of Sr, Fe, and Ni for the as-prepared full cell and the full cell operated in electrolysis mode are displayed in Fig. 8. The complete EDS mappings for the pristine cell (Fig. S5) and the mid-term tested full cell (Fig. S6) can be found in the supplementary. The EDS analyses were intended to provide more information about probable ion diffusion and particle migration during manufacturing and cell operation under SOEC conditions. A comparison of the EDS mappings before and after the degradation test (Fig. 8(a) and (b)) reveals the occurring diffusion of Sr and Fe ions from the STF fuel electrode into the barrier layer. The observation of Fe and Sr diffusion to a similar extent in both, the pristine and the tested cell, leads to the conclusion that this diffusion already occurs during the manufacturing process of the full cell, particularly during the sintering of the fuel electrode at 1050 °C in air. Although there is Sr diffusion from the electrode in the direction of the 8YSZ electrolyte, no formation of SZO phases at the GDC/8YSZ interface on the fuel electrode side can be detected. Based on the EDS mapping of Ni in Fig. 8 (b), it can be concluded that grown, rather spherical particles, which can be detected in the STF fuel electrode and the barrier layer after the stability tests, are Ni particles. This indicates the diffusion of nickel from the NiO contact layer used here in the direction of the electrolyte during the cell's operation. The majority of Ni particles after ca. 1700 h electrolysis operation can be found in the STF fuel electrode.

The diffusion of Ni particles during electrolysis operation could already be observed after a short-term test under the same conditions. The SEM image and the corresponding Ni elemental mapping can be found in Fig. S7. It can be seen that the Ni migration into the STF fuel electrode and the GDC barrier layer already started during the first 125 h of electrolysis operation. A possible influence of the grown Ni particles and their migration on the electrochemical performance and the stability of the cell cannot be excluded and has yet to be determined. Besides the migration of Ni particles into the STF fuel electrode and barrier layer, a possible change in the microstructure of the Ni/NiO contact layer could lead to an alteration in the cell's performance. A simple experiment was set up to investigate the basic influence of the operating conditions at OCV on Ni coarsening/agglomeration. A NiO contact layer was applied on a YSZ/GDC/STF half-cell, which was subsequently heat-treated in 50 % $H_2O$ + 50 % $H_2$ at 800 °C for 2 h and 200 h. After 200 h, coarsening of the particles could be detected; the corresponding laser microscope images can be seen in Fig. S8. This coarsening/agglomeration of the Ni particles could decrease the contact area and increase the measured cell resistance.

## 4. Conclusion

The electrochemical performance of the $Sr_{0.98}Ti_{0.5}Fe_{0.5}O_3$ (STF) fuel electrode was comprehensively studied for its application in steam electrolysis. Therefore, STF powder was synthesized, and solid oxide cells were fabricated in symmetrical and full-cell configurations. The STF material demonstrated good chemical stability in a 50 % $H_2O$ + 50 % $H_2$ atmosphere at 800 °C with only minor formation of $Fe_3O_4$ secondary phase. A high chemical reactivity was observed between the STF perovskite and 8YSZ electrolyte material, while no interactions between STF and GDC could be detected.

Electrochemical analysis revealed that the STF electrode exhibits high electrocatalytic activity for hydrogen oxidation/evolution within the 650–800 °C temperature range. The polarization resistance ($R_p$) remained stable across the 3 %–50 % $H_2O/H_2$ range. However, increasing the steam concentration beyond 50 % led to significant degradation in $R_p$. Notably, at 90 % $H_2O$ + 10 % $H_2$, the polarization resistance increased to approximately four times the mean value observed within the 3%–50 % steam range. A similar trend was observed in the ohmic resistance with rising oxygen partial pressure.

Further interpretation of impedance spectra and analysis of rate-limiting steps in steam electrolysis identified five main processes contributing to overall electrode impedance. A mid-term degradation study for 1700 h at 800 °C using 50 % $H_2O$ + 50 % $H_2$ and i = −0.43 A $cm^{-2}$ resulted in a voltage degradation rate of 195 mV $kh^{-1}$ and showed that the degradation is mainly due to increasing ohmic resistance.

The post-test analysis showed no significant microstructure changes in the STF fuel electrode after 1700 h of electrolysis operation. However, the migration of Ni particles from the current collector into the STF electrode and GDC barrier layer during the operation could be observed.

## CRediT authorship contribution statement

**Franziska E. Winterhalder:** Writing – review & editing, Writing – original draft, Methodology, Investigation, Conceptualization. **Yousef A. Farzin:** Writing – review & editing, Writing – original draft, Investigation. **Yoo Jung Sohn:** Writing – review & editing, Investigation.

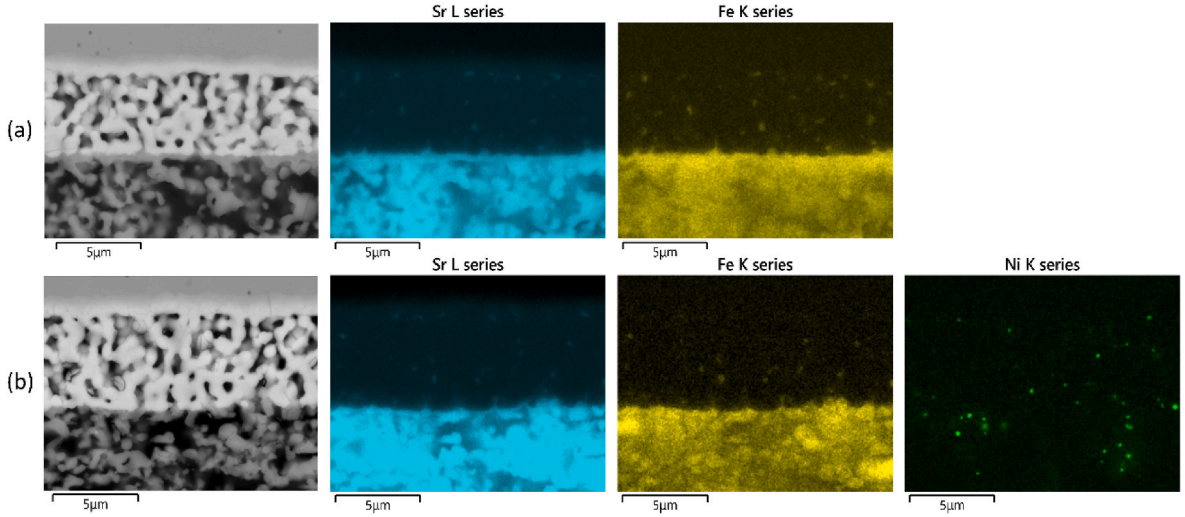


**Fig. 8.** BSE image & EDS elemental mapping of Sr, Fe and Ni in the STF/GDC/YSZ interface of a) the as-prepared full cell and b) full cell tested for ca. 1700 h in electrolysis operation (800 °C, 50 % $H_2O$ + 50 % $H_2$, i = −0.43 A $cm^{-2}$).

**Christian Lenser:** Writing – review & editing, Supervision, Formal analysis. **Doris Sebold:** Writing – review & editing, Investigation. **Olivier Guillon:** Writing – review & editing, Supervision, Resources. **André Weber:** Writing – review & editing, Supervision. **Norbert H. Menzler:** Writing – review & editing, Supervision, Resources, Funding acquisition.

## Declaration of competing interest

The authors declare that they have no known competing financial interests or personal relationships that could have appeared to influence the work reported in this paper.

## Acknowledgements

The authors gratefully acknowledge the basic funding provided by the Federal Ministry of Education and Research (BMBF) through the Helmholtz Association. This project has received funding from the SOC Degradation 2.0 project, which was supported by the BMBF (grant number: 03ST0621). Special thanks to Dr. Michael Müller (IMD-1, FZJ) for the annealing experiments under reducing conditions and Dr. Dylan Jennings (IMD-2, FZJ) for the SEM analysis of the STF powder.

## Appendix A. Supplementary data

Supplementary data to this article can be found online at https://doi.org/10.1016/j.jpowsour.2024.236084.

## Data availability

Data will be made available on request.

## References

[1] S.R. Foit, I.C. Vinke, L.G.J. de Haart, R. Eichel, Power-to-Syngas – eine Schlüsseltechnologie für die Umstellung des Energiesystems? Angew. Chem. 129 (2017) 5488–5498, https://doi.org/10.1002/ange.201607552.
[2] S.E. Wolf, F.E. Winterhalder, V. Vibhu, L.G.J. de Haart, O. Guillon, R.A. Eichel, N. H. Menzler, Solid oxide electrolysis cells - current material development and industrial application, J Mater Chem A Mater 11 (2023) 17977–18028, https://doi.org/10.1039/d3ta02161k.
[3] Y. Zheng, J. Wang, B. Yu, W. Zhang, J. Chen, J. Qiao, J. Zhang, A review of high temperature co-electrolysis of H2O and CO2 to produce sustainable fuels using solid oxide electrolysis cells (SOECs): Advanced materials and technology, Chem. Soc. Rev. 46 (2017) 1427–1463, https://doi.org/10.1039/c6cs00403b.
[4] F. Monaco, M. Hubert, J. Vulliet, J.P. Ouweltjes, D. Montinaro, P. Cloetens, P. Piccardo, F. Lefebvre-Joud, J. Laurencin, Degradation of Ni-YSZ electrodes in solid oxide cells: impact of polarization and initial microstructure on the Ni evolution, J. Electrochem. Soc. 166 (2019) F1229–F1242, https://doi.org/10.1149/2.1261915jes.
[5] Clean Hydrogen Joint Undertaking, Clean Hydrogen Strategic Research and Innovation Agenda 2021-2027, 2022.
[6] M.B. Mogensen, M. Chen, H.L. Frandsen, C. Graves, J.B. Hansen, K.V. Hansen, A. Hauch, T. Jacobsen, S.H. Jensen, T.L. Skafte, X. Sun, Reversible solid-oxide cells for clean and sustainable energy, Clean Energy 3 (2019) 175–201, https://doi.org/10.1093/ce/zkz023.
[7] G. Tsekouras, D. Neagu, J.T.S. Irvine, Step-change in high temperature steam electrolysis performance of perovskite oxide cathodes with exsolution of B-site dopants, Energy Environ. Sci. 6 (2013) 256–266, https://doi.org/10.1039/c2ee22547f.
[8] D.M. Bastidas, S. Tao, J.T.S. Irvine, A symmetrical solid oxide fuel cell demonstrating redox stable perovskite electrodes, J. Mater. Chem. 16 (2006) 1603–1605, https://doi.org/10.1039/b600532b.
[9] W. Li, J. Sunarso, Y. Yang, Y. Chen, C. Ge, W. Wang, Y. Guo, R. Ran, W. Zhou, Strategies for improving oxygen ionic conducting in perovskite oxides and their practical applications, Energy Rev. (2024) 100085, https://doi.org/10.1016/j.enrev.2024.100085.
[10] J. Zhou, L. Xu, C. Ding, C. Wei, Z. Tao, Layered perovskite (PrBa)0.95(Fe0.9Mo0.1) 2O5+δ as electrode materials for high-performing symmetrical solid oxide electrolysis cells, Mater. Lett. 257 (2019), https://doi.org/10.1016/j.matlet.2019.126758.
[11] B. Ge, J.T. Ma, D. Ai, C. Deng, X. Lin, J. Xu, Sr2FeNbO6 applied in solid oxide electrolysis cell as the hydrogen electrode: kinetic studies by comparison with Ni-YSZ, Electrochim. Acta 151 (2015) 437–446, https://doi.org/10.1016/j.electacta.2014.11.078.
[12] Y.A. Farzin, A. Babaei, T.L. Skafte, E. Stamate, A. Ataie, S.H. Jensen, Low-temperature preparation and investigation of electrochemical properties of SFM/CGO composite electrode, Solid State Ion 356 (2020) 5, https://doi.org/10.1016/j.ssi.2020.115435.
[13] Y. Alizad Farzin, A. Babaei, T. Løye Skafte, E. Stamate, A. Ataie, S.H. Jensen, Development of an SFMM/CGO composite electrode with stable electrochemical performance at different oxygen partial pressures, Int. J. Hydrogen Energy 47 (2022) 7915–7931, https://doi.org/10.1016/j.ijhydene.2021.12.104.
[14] Q. Liu, C. Yang, X. Dong, F. Chen, Perovskite Sr2Fe1.5Mo0.5O 6-δ as electrode materials for symmetrical solid oxide electrolysis cells, Int. J. Hydrogen Energy 35 (2010) 10039–10044, https://doi.org/10.1016/j.ijhydene.2010.08.016.
[15] K.-T. Wu, T. Ishihara, Development of highly efficient composite electrodes, CuFe 2 O 4 -La(Sr)Fe(Mn)O 3 , for high-temperature Co-electrolysis of CO 2 -steam, ECS Trans. 103 (2021) 561–567, https://doi.org/10.1149/10301.0561ecst.
[16] T. Ishihara, S. Wang, K.T. Wu, Highly active oxide cathode of La(Sr)Fe(Mn)O3 for intermediate temperature CO2 and CO2-H2O co-electrolysis using LSGM electrolyte, Solid State Ion 299 (2017) 60–63, https://doi.org/10.1016/j.ssi.2016.09.013.
[17] Z. Ma, Y. Li, Y. Zheng, W. Li, X. Chen, X. Sun, X. Chen, J. Zhou, La0.75Sr0.25Cr0.5Mn0.5O3-δ as cathode for electrolysis and co-electrolysis of CO2 and H2O in solid oxide electrolysis cell, Ceram. Int. 47 (2021) 23350–23361, https://doi.org/10.1016/j.ceramint.2021.05.049.
[18] R. Xing, Y. Wang, S. Liu, C. Jin, Preparation and characterization of La 0.75Sr 0.25Cr 0.5Mn 0.5O 3-δ-yttria stabilized zirconia cathode supported solid oxide electrolysis cells for hydrogen generation, J. Power Sources 208 (2012) 276–281, https://doi.org/10.1016/j.jpowsour.2012.02.062.
[19] C. Jin, C. Yang, F. Zhao, D. Cui, F. Chen, La0.75Sr0.25Cr0.5Mn0.5O 3 as hydrogen electrode for solid oxide electrolysis cells, Int. J. Hydrogen Energy 36 (2011) 3340–3346, https://doi.org/10.1016/j.ijhydene.2010.12.085.
[20] J.-H. Zhang, F.-Z. Han, C.-X. Li, S.-L. Zhang, Electrochemical performance investigation of Sr(Ti 1−x Fe x)O 3−δ fuel electrodes with different Fe contents for solid oxide electrochemical cells, J. Electrochem. Soc. 169 (2022) 044520, https://doi.org/10.1149/1945-7111/ac6457.
[21] W.C. Jung, H.L. Tuller, Impedance study of SrTi1-xFexO3-δ (x = 0.05 to 0.80) mixed ionic-electronic conducting model cathode, Solid State Ion 180 (2009) 843–847, https://doi.org/10.1016/j.ssi.2009.02.008.
[22] S. Molin, W. Lewandowska-Iwaniak, B. Kusz, M. Gazda, P. Jasinski, Structural and electrical properties of Sr(Ti, Fe)O 3-δ materials for SOFC cathodes, J. Electroceram. 28 (2012) 80–87, https://doi.org/10.1007/s10832-012-9683-x.
[23] A. Nenning, L. Volgger, E. Miller, L.V. Mogni, S. Barnett, J. Fleig, The electrochemical properties of Sr(Ti,Fe)O 3-δ for anodes in solid oxide fuel cells, J. Electrochem. Soc. 164 (2017) F364–F371, https://doi.org/10.1149/2.1271704jes.
[24] S.L. Zhang, D. Cox, H. Yang, B.K. Park, C.X. Li, C.J. Li, S.A. Barnett, High stability SrTi1-: XFexO3- δ electrodes for oxygen reduction and oxygen evolution reactions, J Mater Chem A Mater 7 (2019) 21447–21458, https://doi.org/10.1039/c9ta07548h.
[25] D.P. Fagg, V.V. Kharton, A.V. Kovalevsky, A.P. Viskup, E.N. Naumovich, J. R. Frade, The stability and mixed conductivity in La and Fe doped SrTiO3 in the search for potential SOFC anode materials, J. Eur. Ceram. Soc. 21 (2001) 1831–1835, https://doi.org/10.1016/S0955-2219(01)00125-X.
[26] J.M. Serra, S. Uhlenbruck, W.A. Meulenberg, H.P. Buchkremer, D. Stöver, Nano-structuring of solid oxide fuel cells cathodes, Top. Catal. (2006) 123–131, https://doi.org/10.1007/s11244-006-0114-6.
[27] D. Klotz, A. Weber, E. Ivers-Tiffée, Practical Guidelines for Reliable electrochemical characterization of solid oxide fuel cells, Electrochim. Acta 227 (2017) 110–126, https://doi.org/10.1016/j.electacta.2016.12.148.
[28] D. Zagorac, H. Müller, S. Ruehl, J. Zagorac, S. Rehme, Recent developments in the Inorganic Crystal Structure Database: theoretical crystal structure data and related features, J. Appl. Crystallogr. (2019) 918–925, https://doi.org/10.1107/S160057671900997X.
[29] M.E. Fleet, The structure of magnetite: Symmetry of cubic spinels, J. Solid State Chem. 62 (1986) 75–82, https://doi.org/10.1016/0022-4596(86)90218-5.
[30] P. Adler, S. Eriksson, Structural properties, Mössbauer spectra, and Magnetism of perovskite-type oxides SrFe1–xTixO3–y, Z. Anorg. Allg. Chem. 626 (2000) 118–124, https://doi.org/10.1002/(SICI)1521-3749(200001)626:1<118::AID-ZAAC118>3.0.CO;2-K.
[31] M. Santaya, C.E. Jiménez, M.D. Arce, E.A. Carbonio, L.M. Toscani, R. Garcia-Diez, A. Knop-Gericke, L.V. Mogni, M. Bär, H.E. Troiani, Exsolution versus particle segregation on (Ni,Co)-doped and undoped SrTi0.3Fe0.7O3-δ perovskites: differences and influence of the reduction path on the final system nanostructure, Int. J. Hydrogen Energy 48 (2023) 38842–38853, https://doi.org/10.1016/j.ijhydene.2023.06.203.
[32] T. Zhu, H.E. Troiani, L.V. Mogni, M. Han, S.A. Barnett, Ni-substituted Sr(Ti,Fe)O3 SOFC anodes: Achieving high performance via metal Alloy nanoparticle exsolution, Joule 2 (2018) 478–496, https://doi.org/10.1016/j.joule.2018.02.006.
[33] A. Nenning, J. Fleig, Electrochemical XPS investigation of metal exsolution on SOFC electrodes: Controlling the electrode oxygen partial pressure in ultra-high-vacuum, Surf. Sci. 680 (2019) 43–51, https://doi.org/10.1016/j.susc.2018.10.006.
[34] F. Schulze-Küppers, S.F.P. Ten Donkelaar, S. Baumann, P. Prigorodov, Y.J. Sohn, H. J.M. Bouwmeester, W.A. Meulenberg, O. Guillon, Structural and functional properties of SrTi1-xFexO3-δ (0 ≤ x ≤ 1) for the use as oxygen transport membrane, Sep. Purif. Technol. 147 (2015) 414–421, https://doi.org/10.1016/j.seppur.2014.12.020.

[35] Y. Jiang, Y. Yang, C. Xia, H.J.M. Bouwmeester, Sr2Fe1.4Mn0.1Mo0.5O6-: δ perovskite cathode for highly efficient CO2 electrolysis, J Mater Chem A Mater 7 (2019) 22939–22949, https://doi.org/10.1039/c9ta07689a.

[36] Y. Li, X. Chen, Y. Yang, Y. Jiang, C. Xia, Mixed-conductor Sr2Fe1.5Mo0.5O6-δ as Robust fuel electrode for pure CO2 reduction in solid oxide electrolysis cell, ACS Sustain Chem Eng 5 (2017) 11403–11412, https://doi.org/10.1021/acssuschemeng.7b02511.

[37] B.J. Kennedy, C.J. Howard, B.C. Chakoumakos, High-temperature Phase Transitions in SrZrO 3, n.d.

[38] M. Yashima, S. Sasaki, M. Kakihana, Y. Yamaguchi, H. Arashi, M. Yoshimura, Oxygen-induced structural change of the tetragonal phase around the tetragonal-cubic phase Boundary in ZrO2-YOl, s Solid Solutions (1994).

[39] W.H. Kim, H.S. Song, J. Moon, H.W. Lee, Intermediate temperature solid oxide fuel cell using (La,Sr)(Co,Fe)O3-based cathodes, Solid State Ion 177 (2006) 3211–3216, https://doi.org/10.1016/j.ssi.2006.07.049.

[40] J. Szász, F. Wankmüller, V. Wilde, H. Störmer, D. Gerthsen, N.H. Menzler, E. Ivers-Tiffée, Nature and Functionality of La 0.58 Sr 0.4 Co 0.2 Fe 0.8 O 3-δ/Gd 0.2 Ce 0.8 O 2-δ/Y 0.16 Zr 0.84 O 2-δ interfaces in SOFCs, J. Electrochem. Soc. 165 (2018) F898–F906, https://doi.org/10.1149/2.0031811jes.

[41] S.E. Wolf, F.E. Winterhalder, V. Vibhu, L.G.J. de Haart, O. Guillon, R.A. Eichel, N. H. Menzler, Solid oxide electrolysis cells - current material development and industrial application, J Mater Chem A Mater 11 (2023) 17977–18028, https://doi.org/10.1039/d3ta02161k.

[42] S.-L. Zhang, H. Wang, T. Yang, M.Y. Lu, C.-X. Li, C.-J. Li, S.A. Barnett, Advanced oxygen-electrode-supported solid oxide electrochemical cells with Sr(Ti,Fe)O3−δ-based fuel electrodes for electricity generation and hydrogen production, J Mater Chem A Mater 8 (2020) 25867–25879, https://doi.org/10.1039/D0TA06678H.

[43] A. Donazzi, T.A. Schmauss, S.A. Barnett, Catalytic and electrocatalytic performance of Sr(Ti0.3Fe0.7Ru0.07)O3-δ for applications in solid oxide fuel cells supplied with ethanol steam reforming mixtures, J. Power Sources 551 (2022) 232215, https://doi.org/10.1016/j.jpowsour.2022.232215.

[44] C. Artini, M. Pani, A. Lausi, R. Masini, G.A. Costa, High temperature structural study of Gd-doped ceria by Synchrotron X-ray diffraction (673 K $\leq$ T $\leq$ 1073 K), Inorg. Chem. 53 (2014) 10140–10149, https://doi.org/10.1021/ic5011242.

[45] D.P. Fagg, V.V. Kharton, A.V. Kovalevsky, A.P. Viskup, E.N. Naumovich, J. R. Frade, The stability and mixed conductivity in La and Fe doped SrTiO3 in the search for potential SOFC anode materials, J. Eur. Ceram. Soc. 21 (2001) 1831–1835, https://doi.org/10.1016/S0955-2219(01)00125-X.

[46] J. Muller, A. Collomb, A new representation of the bipyramidal site in the SrFe12O19 M-type hexagonal ferrite between 4.6 and 295 K, J. Magn. Magn Mater. 103 (1992) 194–203, https://doi.org/10.1016/0304-8853(92)90253-K.

[47] I.V. Shamsutov, O.V. Merkulov, M.V. Patrakeev, SrFe12O19 as an impurity in perovskite-type ferrites, Mater. Lett. 283 (2021), https://doi.org/10.1016/j.matlet.2020.128753.

[48] F. Kamutzki, M.F. Bekheet, S. Schneider, A. Gurlo, D.A.H. Hanaor, A comparison of syntheses approaches towards functional polycrystalline silicate ceramics, Open Ceramics 9 (2022), https://doi.org/10.1016/j.oceram.2022.100241.

[49] A. Majid, J. Tunney, S. Argue, D. Wang, M. Post, J. Margeson, Preparation of SrFeO2.85 perovskite using a citric acid assisted Pechini-type method, J. Alloys Compd. 398 (2005) 48–54, https://doi.org/10.1016/j.jallcom.2005.02.023.

[50] C. Grosselindemann, N. Russner, S. Dierickx, F. Wankmüller, A. Weber, Deconvolution of gas diffusion polarization in Ni/Gadolinium-Doped ceria fuel electrodes, J. Electrochem. Soc. 168 (2021) 124506, https://doi.org/10.1149/1945-7111/AC3D02.

[51] S. Dierickx, A. Weber, E. Ivers-Tiffée, How the distribution of relaxation times enhances complex equivalent circuit models for fuel cells, Electrochim. Acta 355 (2020) 4, https://doi.org/10.1016/j.electacta.2020.136764.

[52] Y. Alizad Farzin, M. Harenbrock, D. Nardini, A. Weber, Enhancing LSCF-based air electrode durability: insights into sulfur poisoning and air purification, Solid State Ion 411 (2024) 116569, https://doi.org/10.1016/J.SSI.2024.116569.

[53] Y. Alizad Farzin, M. Bjerg Mogensen, S. Pirou, H. Lund Frandsen, Perovskite/Ruddlesden-Popper composite fuel electrode of strontium-praseodymium-manganese oxide for solid oxide cells: an alternative candidate, J. Power Sources 580 (2023) 23345, https://doi.org/10.1016/j.jpowsour.2023.233450.

[54] S. Dierickx, T. Mundloch, A. Weber, E. Ivers-Tiffée, Advanced impedance model for double-layered solid oxide fuel cell cermet anodes, J. Power Sources 415 (2019) 69–82, https://doi.org/10.1016/J.JPOWSOUR.2019.01.043.

[55] A. Leonide, V. Sonn, A. Weber, E. Ivers-Tiffée, Evaluation and modeling of the cell resistance in anode-supported solid oxide fuel cells, J. Electrochem. Soc. 155 (2008) B36, https://doi.org/10.1149/1.2801372.

[56] A.M. Hussain, J.V.T. Hogh, W. Zhang, N. Bonanos, Efficient ceramic anodes infiltrated with binary and ternary electrocatalysts for SOFCs operating at low temperatures, J. Power Sources 216 (2012) 308–313, https://doi.org/10.1016/j.jpowsour.2012.05.036.

[57] Y.A. Alizad Farzin, M. Harenbrock, D. Nardini, A. Weber, Enhancing LSCF-based air electrode durability: insights into sulfur poisoning and air purification, Solid State Ion 411 (2024), https://doi.org/10.1016/j.ssi.2024.116569. Art.-Nr.

[58] Y. Alizad Farzin, M. Bjerg Mogensen, S. Pirou, H. Lund Frandsen, Perovskite/Ruddlesden-Popper composite fuel electrode of strontium-praseodymium-manganese oxide for solid oxide cells: an alternative candidate, J. Power Sources 580 (2023) 233450, https://doi.org/10.1016/j.jpowsour.2023.233450.

[59] D.A. Osinkin, N.I. Lobachevskaya, A.Yu Suntsov, The electrochemical behavior of the promising Sr2Fe1.5Mo0.5O6–δ + Ce0.8Sm0.2O1.9–δ anode for the intermediate temperature solid oxide fuel cells, J. Alloys Compd. 708 (2017) 451–455, https://doi.org/10.1016/j.jallcom.2017.03.057.

[60] F. Meng, T. Xia, J. Wang, Z. Shi, H. Zhao, Praseodymium-deficiency Pr0.94BaCo2O6-δ double perovskite: a promising high performance cathode material for intermediate-temperature solid oxide fuel cells, J. Power Sources 293 (2015) 741–750, https://doi.org/10.1016/j.jpowsour.2015.06.007.

[61] W.G. Bessler, M. Vogler, H. Störmer, D. Gerthsen, A. Utz, A. Weber, E. Ivers-Tiffée, Model anodes and anode models for understanding the mechanism of hydrogen oxidation in solid oxide fuel cells, Phys. Chem. Chem. Phys. 12 (2010) 13888–13903, https://doi.org/10.1039/C0CP00541J.

[62] S. Kanae, Y. Toyofuku, T. Kawabata, Y. Inoue, T. Daio, J. Matsuda, J.-T. Chou, Y. Shiratori, S. Taniguchi, K. Sasaki, Microstructural characterization of SrZrO3 formation and the influence to SOFC performance, ECS Trans. 68 (2015) 2463, https://doi.org/10.1149/06801.2463ecst.

[63] S. Golani, F. Wankmüller, W. Herzhof, C. Dellen, N.H. Menzler, A. Weber, Impact of GDC interlayer microstructure on strontium zirconate Interphase formation and cell performance, J. Electrochem. Soc. 170 (2023) 104501, https://doi.org/10.1149/1945-7111/ACFC2C.

[64] J. Zamudio-García, L. Caizán-Juanarena, J.M. Porras-Vázquez, E.R. Losilla, D. Marrero-López, A review on recent advances and trends in symmetrical electrodes for solid oxide cells, J. Power Sources 520 (2022) 230852, https://doi.org/10.1016/j.jpowsour.2021.230852.

[65] F. Kullmann, A. Schwiers, M. Juckel, N.H. Menzler, A. Weber, Enhancement of performance and sulfur Tolerance of ceria-based fuel electrodes in low temperature SOFC, J. Electrochem. Soc. 171 (2024) 044511, https://doi.org/10.1149/1945-7111/ad3ebd.

[66] Y.A. Farzin, A. Weber, M. Harenbrock, D. Nardini, Effective Suppression of LSCF air electrode degradation by air Cleaning, ECS Trans. 111 (2023) 1987, https://doi.org/10.1149/11106.1987ECST.

[67] X. Sun, P.V. Hendriksen, M.B. Mogensen, M. Chen, Degradation in solid oxide electrolysis cells during long term testing, Fuel Cell. 19 (2019) 740–747, https://doi.org/10.1002/fuce.201900081.

[68] S. Primdahl, M. Mogensen, Gas conversion impedance: a test Geometry effect in characterization of solid oxide fuel cell anodes, J. Electrochem. Soc. 145 (1998) 2431, https://doi.org/10.1149/1.1838654.

[69] A. Leonide, V. Sonn, A. Weber, E. Ivers-Tiffée, Evaluation and modeling of the cell resistance in anode-supported solid oxide fuel cells, J. Electrochem. Soc. 155 (2008) B36, https://doi.org/10.1149/1.2801372.

[70] T. Zhu, D. Fowler, K. Poeppelmeier, M. Han, S. Barnett, Hydrogen oxidation mechanisms on perovskite solid oxide fuel cell anodes, J. Electrochem. Soc. 163 (2016) F952–F961, https://doi.org/10.1149/2.1321608jes.

[71] Özden Çelikbilek, E. Siebert, D. Jauffrès, C.L. Martin, E. Djurado, Influence of sintering temperature on morphology and electrochemical performance of LSCF/GDC composite films as efficient cathode for SOFC, Electrochim. Acta 246 (2017) 1248–1258, https://doi.org/10.1016/j.electacta.2017.06.070.

[72] Y. Alizad Farzin, A. Babaei, T. Løye Skafte, E. Stamate, A. Ataie, S.H. Jensen, Development of an SFMM/CGO composite electrode with stable electrochemical performance at different oxygen partial pressures, Int. J. Hydrogen Energy 47 (2022) 7915–7931, https://doi.org/10.1016/j.ijhydene.2021.12.104.

[73] M. Chen, D. Chen, M. Chang, H. Hu, Q. Xu, New insight into hydrogen oxidation reaction on La0.3Sr0.7Fe0.7Cr0.3O3-δ perovskite as a solid oxide fuel cell anode, J. Electrochem. Soc. 164 (2017) F405, https://doi.org/10.1149/2.1571704jes.

[74] Q.X. Fu, F. Tietz, D. Stöver, La0.4Sr0.6Ti1 − x Mnx O3 − δ perovskites as anode materials for solid oxide fuel cells, J. Electrochem. Soc. 153 (2006) D74, https://doi.org/10.1149/1.2170585.

[75] C. Endler-Schuck, J. Joos, C. Niedrig, A. Weber, E. Ivers-Tiffée, The chemical oxygen surface exchange and bulk diffusion coefficient determined by impedance spectroscopy of porous La0.58Sr0.4Co0.2Fe0.8O3−δ (LSCF) cathodes, Solid State Ion 269 (2015) 67–79, https://doi.org/10.1016/j.ssi.2014.11.018.

[76] C. Graves, S.D. Ebbesen, M. Mogensen, Co-electrolysis of CO2 and H2O in solid oxide cells: performance and durability, Solid State Ion 192 (2011) 398–403, https://doi.org/10.1016/j.ssi.2010.06.014.

[77] S. Golani, F. Wankmüller, W. Herzhof, C. Dellen, N.H. Menzler, A. Weber, Impact of GDC interlayer microstructure on strontium zirconate Interphase formation and cell performance, J. Electrochem. Soc. 170 (2023) 104501, https://doi.org/10.1149/1945-7111/acfc2c.

[78] S.P.S. Badwal, Zirconia-based solid electrolytes: microstructure, stability and ionic conductivity, Solid State Ion 52 (1992) 23–32, https://doi.org/10.1016/0167-2738(92)90088-7.

[79] M. Hattori, Y. Takeda, Y. Sakaki, A. Nakanishi, S. Ohara, K. Mukai, J.-H. Lee, T. Fukui, Effect of aging on conductivity of yttria stabilized zirconia, J. Power Sources 126 (2004) 23–27, https://doi.org/10.1016/j.jpowsour.2003.08.018.

[80] P. Khajavi, P.V. Hendriksen, J. Chevalier, L. Gremillard, H.L. Frandsen, Improving the fracture toughness of stabilized zirconia-based solid oxide cells fuel electrode supports: effects of type and concentration of stabilizer(s), J. Eur. Ceram. Soc. 40 (2020) 5670–5682, https://doi.org/10.1016/j.jeurceramsoc.2020.05.042.

[81] M. Ghatee, J.T.S. Irvine, Investigation of electrical and mechanical properties of tetragonal/cubic zirconia composite electrolytes prepared through stabilizer coating method, Int. J. Hydrogen Energy 35 (2010) 9427–9433, https://doi.org/10.1016/j.ijhydene.2010.02.120.

[82] L.-W. Tai, M.M. Nasrallah, H.U. Anderson, D.M. Sparlin, S.R. Sehlin, Structure and electrical properties of La1 − xSrxCo1 − yFeyO3. Part 2. The system La1 − xSrxCo0.2Fe0.8O3, Solid State Ion 76 (1995) 273–283, https://doi.org/10.1016/0167-2738(94)00245-N.

[83] K. Huang, H.Y. Lee, J.B. Goodenough, Sr- and Ni-doped LaCoO3 and LaFeO3 perovskites: new cathode materials for solid-oxide fuel cells, J. Electrochem. Soc. 145 (1998) 3220, https://doi.org/10.1149/1.1838789.

[84] S.P. Jiang, Development of lanthanum strontium cobalt ferrite perovskite electrodes of solid oxide fuel cells – a review, Int. J. Hydrogen Energy 44 (2019) 7448–7493, https://doi.org/10.1016/j.ijhydene.2019.01.212.
[85] F. Monaco, D. Ferreira-Sanchez, M. Hubert, B. Morel, D. Montinaro, D. Grolimund, J. Laurencin, Oxygen electrode degradation in solid oxide cells operating in electrolysis and fuel cell modes: LSCF destabilization and interdiffusion at the electrode/electrolyte interface, Int. J. Hydrogen Energy 46 (2021) 31533–31549, https://doi.org/10.1016/j.ijhydene.2021.07.054.
[86] S.-S. Liu, K. Develos-Bagarinao, R.A. Budiman, T. Ishiyama, H. Kishimoto, K. Yamaji, Towards an atomic scale understanding of the early-stage deterioration mechanism of LSCF, J Mater Chem A Mater 11 (2023) 21983–22000, https://doi.org/10.1039/D3TA04585D.
[87] J. Szász, F. Wankmüller, V. Wilde, H. Störmer, D. Gerthsen, N.H. Menzler, E. Ivers-Tiffée, Nature and Functionality of La 0.58 Sr 0.4 Co 0.2 Fe 0.8 O 3-δ/Gd 0.2 Ce 0.8 O 2-δ/Y 0.16 Zr 0.84 O 2-δ interfaces in SOFCs, J. Electrochem. Soc. 165 (2018) F898–F906, https://doi.org/10.1149/2.0031811jes.
[88] R. Kiebach, W. Zhang, M. Chen, K. Norrman, H.J. Wang, J.R. Bowen, R. Barfod, P. V. Hendriksen, W. Zhang, Stability of La0.6Sr0.4Co0.2Fe0.8O3/Ce0.9Gd0.1O2 cathodes during sintering and solid oxide fuel cell operation, J. Power Sources 283 (2015) 151–161, https://doi.org/10.1016/j.jpowsour.2015.02.064.
[89] J. Laurencin, M. Hubert, D.F. Sanchez, S. Pylypko, M. Morales, A. Morata, B. Morel, D. Montinaro, F. Lefebvre-Joud, E. Siebert, Degradation mechanism of La0.6Sr0.4Co0.2Fe0.8O3-δ/Gd0.1Ce0.9O2-δ composite electrode operated under solid oxide electrolysis and fuel cell conditions, Electrochim. Acta 241 (2017) 459–476, https://doi.org/10.1016/j.electacta.2017.05.011.
[90] I.D. Unachukwu, V. Vibhu, I.C. Vinke, R.A. Eichel, L.G.J. (Bert) de Haart, Electrochemical and degradation behaviour of single cells comprising Ni-GDC fuel electrode under high temperature steam- and co-electrolysis conditions, J. Power Sources 556 (2023), https://doi.org/10.1016/j.jpowsour.2022.232436.
[91] K. Chen, S.P. Jiang, Surface segregation in solid oxide cell oxygen electrodes: phenomena, Mitigation Strategies and electrochemical properties, Electrochem. Energy Rev. 3 (2020) 730–765, https://doi.org/10.1007/s41918-020-00078-z.
[92] E. Mercadelli, A. Gondolini, M. Ardit, G. Cruciani, C. Melandri, S. Escolástico, J. M. Serra, A. Sanson, Chemical and mechanical stability of BCZY-GDC membranes for hydrogen separation, Sep. Purif. Technol. 289 (2022), https://doi.org/10.1016/j.seppur.2022.120795.
[93] T.P. Mishra, A.M. Laptev, M. Ziegner, S.K. Sistla, A. Kaletsch, C. Broeckmann, O. Guillon, M. Bram, Field-assisted sintering/spark plasma sintering of gadolinium-doped ceria with controlled re-oxidation for crack prevention, Materials 13 (2020), https://doi.org/10.3390/ma13143184.